Efficient collective swimming by harnessing vortices through deep reinforcement learning

Siddhartha Verma[a,1], Guido Novati[a,1], and Petros Koumoutsakos[a,2]

[a]Computational Science and Engineering Laboratory, ETH Zürich, CH-8092 Zürich, Switzerland

Edited by James A. Sethian, University of California, Berkeley, CA, and approved April 25, 2018 (received for review January 22, 2018)

Fish in schooling formations navigate complex flow fields replete with mechanical energy in the vortex wakes of their companions. Their schooling behavior has been associated with evolutionary advantages including energy savings, yet the underlying physical mechanisms remain unknown. We show that fish can improve their sustained propulsive efficiency by placing themselves in appropriate locations in the wake of other swimmers and intercepting judiciously their shed vortices. This swimming strategy leads to collective energy savings and is revealed through a combination of high-fidelity flow simulations with a deep reinforcement learning (RL) algorithm. The RL algorithm relies on a policy defined by deep, recurrent neural nets, with long–short-term memory cells, that are essential for capturing the unsteadiness of the two-way interactions between the fish and the vortical flow field. Surprisingly, we find that swimming in-line with a leader is not associated with energetic benefits for the follower. Instead, "smart swimmer(s)" place themselves at off-center positions, with respect to the axis of the leader(s) and deform their body to synchronize with the momentum of the oncoming vortices, thus enhancing their swimming efficiency at no cost to the leader(s). The results confirm that fish may harvest energy deposited in vortices and support the conjecture that swimming in formation is energetically advantageous. Moreover, this study demonstrates that deep RL can produce navigation algorithms for complex unsteady and vortical flow fields, with promising implications for energy savings in autonomous robotic swarms.

fish schooling | deep reinforcement learning | autonomous navigation | energy harvesting | recurrent neural networks

There is a long-standing interest for understanding and exploiting the physical mechanisms used by active swimmers in nature (nektons) (1–4). Fish schooling, in particular, one of the most striking patterns of collective behavior and complex decision-making in nature, has been the subject of intense investigation (5–9). A key issue in understanding fish-schooling behavior, and its potential for engineering applications (10), is the clarification of the role of the flow environment. Fish sense and navigate in complex flow fields full of mechanical energy that is distributed across multiple scales by vortices generated by obstacles and other swimming organisms (11, 12). There is evidence that their swimming behavior adapts to flow gradients (rheotaxis), and, in certain cases, it reflects energy-harvesting from such environments (13, 14). Hydrodynamic interactions have also been implicated in the fish-schooling patterns that form when individual fish adapt their motion to that of their peers, while compensating for flow-induced displacements. Recent experimental studies have argued that fish may interact beneficially with each other (9, 15, 16), but in ways that challenge (17) the earlier proposed mechanisms (5, 6) governing fish schooling. However, the role of hydrodynamics in fish schooling is not embraced universally (8, 18, 19), and there is limited quantitative information regarding the physical mechanisms that would explain such energetic benefits. Experimental (15, 16) and computational (20) studies of collective swimming have been hampered by the presence of multiple deforming bodies and their interactions with the flow field. Moreover, numerical simulations have demonstrated that a coherent swimming group cannot be sustained without exerting some form of control strategy on the swimmers (21, 22). Here, we use deep reinforcement learning [deep RL (23)] to discover such strategies for two autonomous and self-propelled swimmers and elucidate the physical mechanisms that enable efficient and sustained coordinated swimming.

During fish propulsion, body undulations and the sideways displacement of the caudal fin generate and inject a series of vortex rings in its wake (24–26). When fish swim in formation, these vortices may assist the locomotion of fish that intercept them judiciously, which in turn can reduce the collective swimming effort. Such vortex-induced benefits have been observed in trout, which curtail muscle use by capitalizing on energy injected in the flow by obstacles present in streams (13, 27). Here, we examine configurations of two and three self-propelled swimmers in a leader(s) –follower(s) arrangement and investigate the physical mechanisms that lead to energetically beneficial interactions by considering four distinct scenarios. Two of these involve smart followers that can make autonomous decisions when interacting with a leader's wake and are referred to as interacting swimmers (*IS*) (e.g., the follower in Fig. 1). Additionally, we consider two distinct solitary swimmers (*SS*) that swim in isolation in an unbounded domain. In the case of interacting swimmers, IS_η denotes swimmers that learn the most efficient way of swimming in the leader's wake (without any positional constraints) and acquire a policy π_η in the process. In turn, swimmer IS_d attempts to minimize lateral deviations from the leader's path, resulting in a locally optimal policy π_d. These autonomous

Significance

Can fish reduce their energy expenditure by schooling? We answer affirmatively this longstanding question by combining state-of-the-art direct numerical simulations of the 3D Navier–Stokes equations with reinforcement learning, using recurrent neural networks with long short-term memory cells to account for the unsteadiness of the flow field. Surprisingly, we find that swimming behind a leader is not always associated with energetic benefits for the follower. In turn, we demonstrate that fish can improve their sustained propulsive efficiency by placing themselves at appropriate locations in the wake of other swimmers and intercepting their wake vortices judiciously. The results show that autonomous, "smart" swimmers may exploit unsteady flow fields to reap substantial energetic benefits and have promising implications for robotic swarms.

Author contributions: S.V., G.N., and P.K. designed research; G.N. performed research; S.V. analyzed data; and S.V., G.N., and P.K. wrote the paper.

The authors declare no conflict of interest.

This article is a PNAS Direct Submission.

[1]S.V. and G.N. contributed equally to this work.

[2]To whom correspondence should be addressed. Email: petros@ethz.ch.

This article contains supporting information online at www.pnas.org/lookup/suppl/doi:10.1073/pnas.1800923115/-/DCSupplemental.

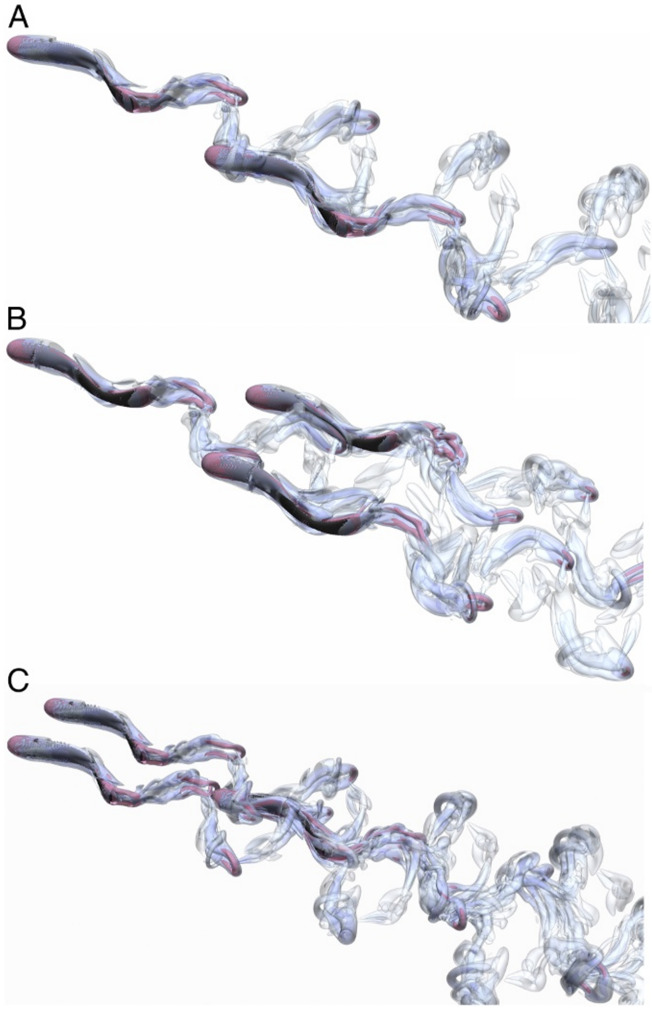

Fig. 1. Efficient coordinated swimming of two and three swimmers. (*A*) DNS of two swimmers, in which the leader swims steadily and the follower maintains a specified relative position such that it increases its efficiency by interacting with one row of the vortex rings shed by the leader. The flow is visualized by isosurfaces of the Q criterion (28). (*B*) DNS of three swimmers, where the two followers maintain specified positions that increase their efficiency by interacting with both rows of the vortex rings shed by the leader. (*C*) DNS of three swimmers with the follower benefitting from one row of wake vortices generated by each leader. Animations of the 3D simulations are provided in Movies S1–S3.

swimmers take decisions by virtue of deep RL, using visual cues from their environment (Fig. 2*A*). The solitary swimmers SS_η and SS_d execute actions identical to IS_η and IS_d, respectively, and serve as "control" configurations to assess how the absence of a leader's wake impacts swimming-energetics.

Deep RL for Swimmers

RL (29) has been introduced to identify navigation policies in several model systems of vortex dipoles, soaring birds and microswimmers (30–32). These studies often rely on simplified representations of organisms interacting with their environment, which allows them to model animal locomotion with reduced physical complexity and manageable computational cost. However, the simplifying assumptions inherent in such models often do not account for feedback of the animals' motion on the environment. High-fidelity numerical simulations, although significantly more computationally demanding, can account for such important considerations to a greater extent, for instance, by allowing flapping or swimming motions that closely mimic the interaction of real animals with their environment. This makes them invaluable for investigating concepts that may be carried over readily to bioinspired robotic applications, with minimal modification. This consideration has motivated our present study, where we expand on our earlier work (33), combining RL with direct numerical simulations (DNSs) of the Navier–Stokes (NS) equations for self-propelled autonomous swimmers. We first investigate 2D swimmers in a tandem configuration to scrutinize the strategy adopted by the RL algorithm for attaining the specified goals. Based on the observed behavior and the physical intuition we gain from examining these smart swimmers, we formulate simplified rules for implementing active control in significantly more complex 3D systems. This reverse-engineering approach allows us to determine simple and effective control rules from a data-driven perspective, without having to rely on simplistic models which may introduce errors owing to underlying assumptions.

Efficient Autonomous Swimmers

We first analyze the kinematics of swimmers IS_η and IS_d (Fig. 2), which were described previously, and were trained to attain specific high-level objectives via deep RL (see *Methods* for details). In both cases, the swimmer trails a leader representing an adult zebrafish of length L, swimming steadily at a velocity U, with tail-beat period T [Reynolds number $Re = L^2/(T\nu) \approx 5000$]. After training, we observe that IS_d is able to maintain its position behind the leader quite effectively ($\Delta y \approx 0$; Fig. 2*D*), in accordance to its reward ($R_d = 1 - |\Delta y|/L$). Surprisingly, IS_η with a reward function proportional to swimming efficiency ($R_\eta = \eta$), also settles close to the center of the leader's wake (Fig. 2*D* and Movie S4), although it receives no reward related to its relative position. This decision to interact actively with the unsteady wake has significant energetic implications, as described later in the text. Both IS_d and IS_η maintain a distance of $\Delta x \approx 2.2L$ from their respective leaders (Fig. 2*C*). IS_η shows a greater proclivity to maintain this separation and intercepts the periodically shed wake vortices just after they have been fully formed and detach from the leader's tail. In addition to $\Delta x = 2.2L$, there is an additional point of stability at $\Delta x = 1.5$ (Fig. 2*E*). The difference $0.7L$ matches the distance between vortices in the wake of the leader. In both positions, the lateral motion of the follower's head is synchronized with the flow velocity in the leader's wake, thus inducing minimal disturbance on the oncoming flow field. We note that a similar synchronization with the flow velocity has been observed when trout minimize muscle use by interacting with vortex columns in a cylinder's wake (13). IS_η undergoes relatively minor body deformation while maneuvering (Fig. 2*F*), whereas IS_d executes aggressive turns involving large body curvature. Trout interacting with cylinder wakes exhibit increased body curvature (27), which is contrary to the behavior displayed by IS_η. The difference may be ascribed to the widely spaced vortex columns generated by large-diameter cylinders used in the experimental study; weaving in and out of comparatively smaller vortices generated by like-sized fish encountered in a school (Fig. 2*B*) would entail excessive energy consumption.

We note that maintaining $\Delta y = 0$ requires significant effort by IS_d (*SI Appendix*, Fig. S2*D*), which is expected, as this swimmer's reward (R_d) is insensitive to energy expenditure. One of our previous studies (33) demonstrated that minimizing lateral displacement led to enhanced swimming efficiency (compared with the leader), albeit with noticeable deviation from $\Delta y = 0$. This conclusion is markedly different from our current observation and can be attributed to the use of improved learning techniques which are better able to achieve the specified goal. In the present study, recurrent neural networks augmented with "long short-term memory" cells (*SI Appendix*, Fig. S3) help encode time dependencies in the value function and

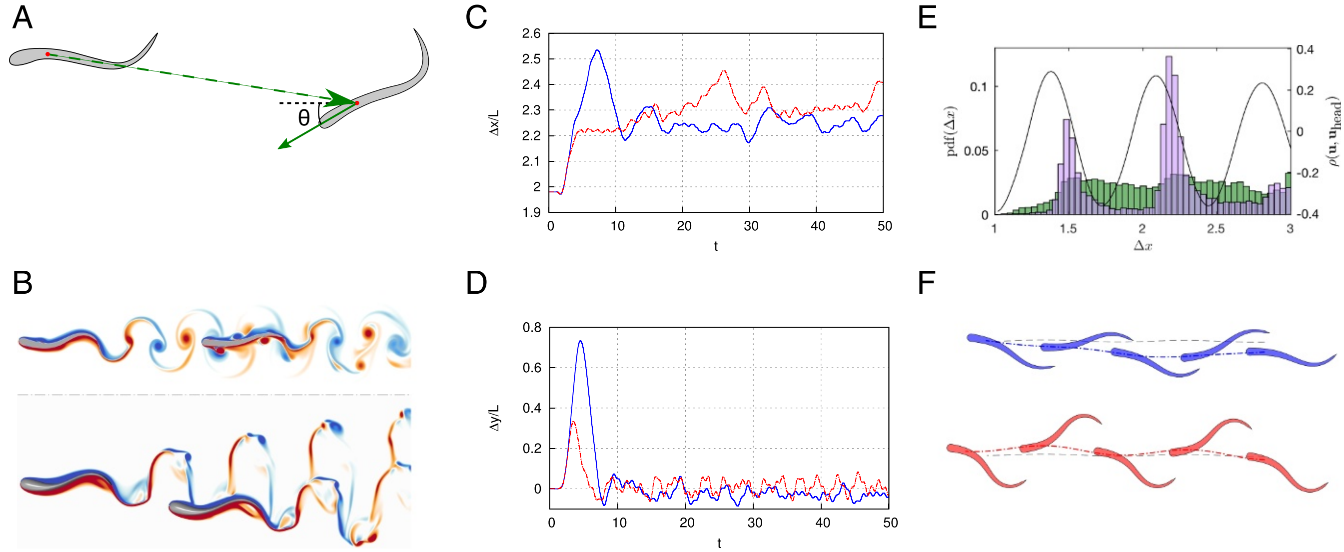

Fig. 2. Learning efficient swimming strategies: Differences between 2D and 3D flow fields. (*A*) The smart swimmer relies on a predefined set of variables to identify its "observed state" (such as range and bearing relative to the leader that are depicted). Additional observed-state parameters are described in *Methods*. (*B*) Comparison of vorticity field in the wake of 2D (*Upper*) and cross-section of the 3D (*Lower*) swimmers (red, positive; blue, negative). In 2D, the leader's wake vortices are aligned with its centerline. In contrast, in 3D flows, the wake vortices are diverging, leaving a quiescent region behind the leader. In 2D, smart followers must align with the leader's centerline. In 3D, they must orient themselves at an angle to harness the wake vortex rings (WRs). Every half a tail-beat period, the smart follower in 2D simulations (IS_η) autonomously selects the most appropriate action encoded in policy π_η learned during training simulations, which allows it to maximize long-term swimming efficiency (Movie S4). The smart follower is capable of adapting to deviations in the leader's trajectory (Movie S5), as these situations are encountered when performing random actions during training. (*C*) Relative horizontal displacement of the smart followers with respect to the leader, over a duration of 50 tail-beat periods starting from rest (solid blue line, IS_η; dash-dot red line, IS_d). (*D*) Lateral displacement of the smart followers. (*E*) Histogram showing the probability density function (PDF; left vertical axis) of swimmer IS_η's preferred center-of-mass location during training. In the early stages of training (first 10,000 transitions; green bars), the swimmer does not show a strong preference for maintaining any particular separation distance. Toward the end of training (last 10,000 transitions; lilac bars), the swimmer displays a strong preference for maintaining a separation distance of either $\Delta x = 1.5L$ or $2.2L$. The solid black line depicts the correlation coefficient, with peaks in the black curve signifying locations where the smart follower's head movement would be synchronized with the flow velocity in an undisturbed wake (see *SI Appendix* for relevant details). (*F*) Comparison of body deformation for swimmers IS_η (*Upper*) and IS_d (*Lower*), from $t = 27$ to $t = 29$. Their respective trajectories are shown with the dash-dot lines, whereas the dashed gray line represents the trajectory of the leader. A quantitative comparison of body curvature for the two swimmers may be found in *SI Appendix*, Fig. S1.

produce far more robust smart swimmers than simpler feedforward networks (33). The performance of our deep recurrent network is compared with that of a feedforward network in *SI Appendix*, Fig. S4 and indicates that the deep network is better able to achieve the goal of in-line following, but at the penalty of increased energy expenditure. As a result, IS_d succeeds in correcting for oscillations about $\Delta y = 0$ much more effectively by undergoing severe body undulations (Fig. 2*F*), leading to increased costs (*SI Appendix*, Fig. S2). These observations confirm that following a leader indiscriminately can be disadvantageous if energetic considerations are not taken into account. Thus, it is unlikely that strict in-line swimming is used as a collective-swimming strategy in nature, and fish presumably adopt a strategy closer to that of IS_η, by coordinating their motion with the wake flow. We note that patterns similar to the ones reported in this study have been observed in a recent experimental study (17). The behavior of swimmer IS_η is also compared qualitatively to that of a real fish following a companion in Movie S6, and we observe that the motion of IS_η resembles the swimming behavior of the live follower quite well.

Intercepting Vortices for Efficient Swimming

To determine the impact of wake-induced interactions on swimming performance, we compare energetics data for IS_η and SS_η in Fig. 3. The swimming efficiency of IS_η is significantly higher than that of SS_η (Fig. 3*A*), and the cost of transport (CoT), which represents energy spent for traversing a unit distance, is lower (Fig. 3*B*). Over a duration of 10 tail-beat periods (from $t = 20$ to $t = 30$; *SI Appendix*, Fig. S2) IS_η experiences a 11% increase in average speed compared with SS_η, a 32% increase in average swimming efficiency and a 36% decrease in CoT. The benefit for IS_η results from both a 29% reduction in effort required for deforming its body against flow-induced forces (P_{Def}) and a 53% increase in average thrust power (P_{Thrust}). Performance differences between IS_η and SS_η exist solely due to the presence/absence of a preceding wake, since both swimmers undergo identical body undulations throughout the simulations. Comparing the swimming efficiency and power values of four distinct swimmers (*SI Appendix*, Fig. S2 and Table S1), we confirm that IS_η and SS_η are considerably more energetically efficient than either IS_d or SS_d.

The efficient swimming of IS_η [e.g., point $\eta_{max}(A)$ in Fig. 3*A*] is attributed to the synchronized motion of its head with the lateral flow velocity generated by the wake vortices of the leader (Movie S4v). This mechanism is evidenced by the correlation curve shown in Fig. 2*E* and by the coalignment of velocity vectors close to the head in Fig. 4 *A* and *B*. As shown in Movie S7, IS_η intercepts the oncoming vortices in a slightly skewed manner, splitting each vortex into a stronger (W_{1U}, Fig. 4*A*) and a weaker fragment (W_{1L}). The vortices interact with the swimmer's own boundary layer to generate "lifted vortices" (L_1), which in turn generate secondary vorticity (S_1) close to the body. Meanwhile, the wake and lifted vortices created during the previous half-period, W_{2U}, W_{2L}, and L_2, have traveled downstream along the body. This sequence of events alternates periodically between the upper (right lateral) and lower (left lateral) surfaces, as seen in Movie S7. Interactions of IS_η with the flow field at

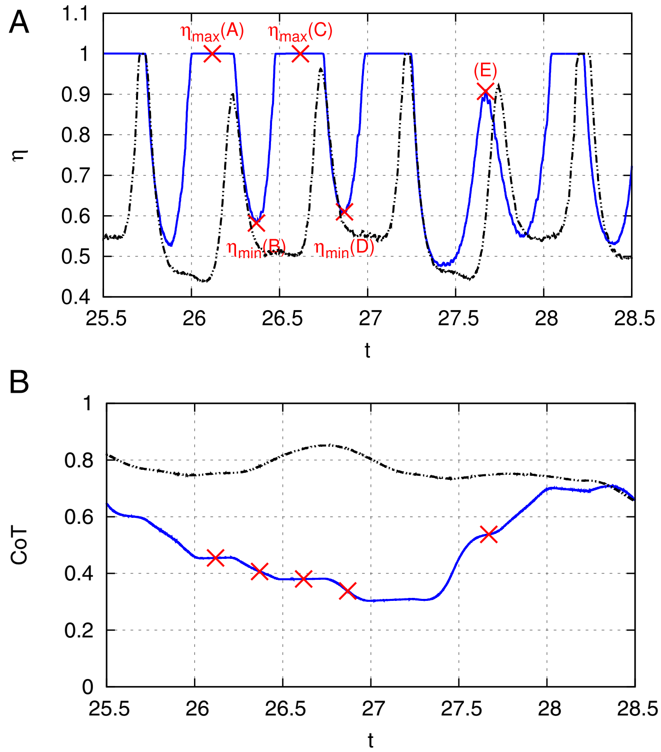

Fig. 3. Energetics data for a smart follower maximizing its swimming efficiency. Swimming efficiency (*A*) and CoT (*B*) for IS_η (solid blue line) and SS_η (dash-double-dot black line), normalized with respect to the CoT of a steady solitary swimmer. Four instances of maximum and minimum efficiency, which occur periodically throughout the simulation at times ($nT_p + 0.12$), ($nT_p + 0.37$), ($nT_p + 0.62$), ($nT_p + 0.87$), have been highlighted. $T_p = 1$ denotes the constant tail-beat period of the swimmers, whereas n represents an integral multiple. The decline in η at point *E* ($t \approx 27.7$, $\eta = 0.86$) results from an erroneous maneuver at $t \approx 26.5$ (Movie S7), which reveals the existence of a time delay between actions and their consequences.

points $\eta_{min}(D)$ and (E) in Fig. 3*A* are analyzed separately in *SI Appendix*, Figs. S5 and S6.

We observe that the swimmer's upper surface is covered in a layer of negative vorticity (and vice versa for the lower surface) (Fig. 4 *A*, *Upper*) owing to the no-slip boundary condition. The wake or the lifted vortices weaken this distribution by generating vorticity of opposite sign (e.g., secondary vorticity visible in narrow regions between the fish surface and vortices L_1, W_{1L}, L_2, and L_3) and create high-speed areas visible as bright spots in Fig. 4 *A*, *Lower*. The resulting low-pressure region exerts a suction force on the surface of the swimmer (Fig. 4 *B*, *Upper*), which assists body undulations when the force vectors coincide with the deformation velocity (Fig. 4 *B*, *Lower*) or increases the effort required when they are counteraligned. The detailed impact of these interactions is demonstrated in Fig. 4 *C*–*F*. On the lower surface, W_{1L} generates a suction force oriented in the same direction as the deformation velocity ($0 < s < 0.2L$ in Fig. 4*B*), resulting in negative P_{Def} (Fig. 4*E*) and favorable P_{Thrust} (Fig. 4*F*). On the upper surface, the lifted vortex L_1 increases the effort required for deforming the body (positive peak in Fig. 4*C* at $s = 0.2L$), but is beneficial in terms of producing large positive thrust power (Fig. 4*D*). Moreover, as L_1 progresses along the body, it results in a prominent reduction in P_{Def} over the next half-period, similar to the negative peak produced by the lifted vortex L_2 ($s = 0.55L$ in Fig. 4*E*). The average P_{Def} on both the upper and lower surfaces is predominantly negative (i.e., beneficial), in contrast to the minimum swimming efficiency instance $\eta_{min}(D)$, where a mostly positive P_{Def} distribution signifies substantial effort required for deforming the body (*SI Appendix*, Fig. S5). We observe noticeable drag on the upper surface close to $s = 0$ (Fig. 4 *B*, *Upper* and Fig. 4*D*), attributed to the high-pressure region forming in front of the swimmer's head. Forces induced by W_{1L} are both beneficial and detrimental in terms of generating thrust power ($0 < s < 0.2L$ in Fig. 4*F*), whereas forces induced by L_2 primarily increase drag but assist in body deformation (Fig. 4*E*). The tail section ($s = 0.8L$ to $1L$) does not contribute noticeably to either thrust or deformation power at the instant of maximum swimming efficiency.

Energy-Saving Mechanisms in Coordinated Swimming

The most discernible behavior of IS_η is the synchronization of its head movement with the wake flow. However, the most prominent reduction in deformation power occurs near the midsection of the body ($0.4 \le s \le 0.7$ in Fig. 4 *C* and *E*). This indicates that the technique devised by IS_η is markedly different from energy-conserving mechanisms implied in theoretical (6, 34) and computational (20) work, namely, drag reduction attributed to reduced relative velocity in the flow and thrust increase owing to the "channelling effect." In fact, the predominant energetics gain (i.e., negative P_{Def}) occurs in areas of high

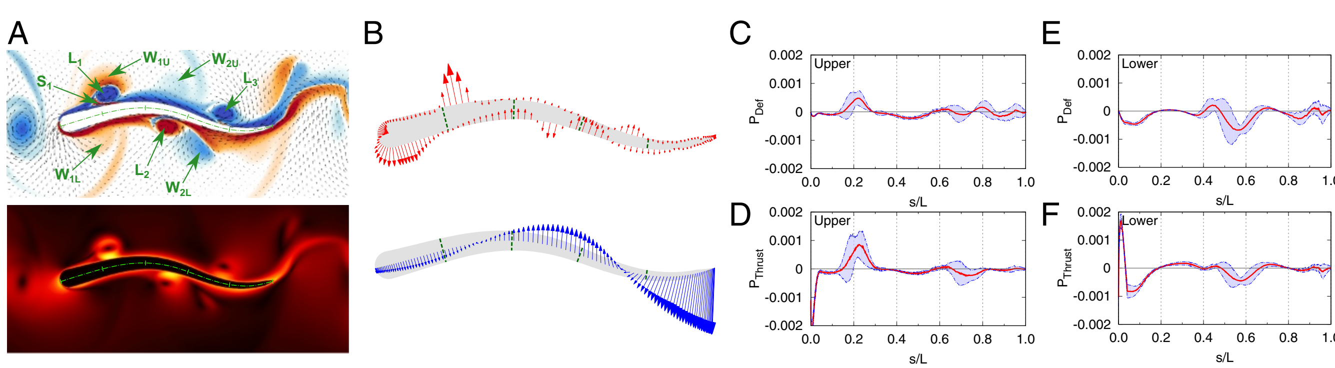

Fig. 4. Flow field and flow-induced forces for IS_η, corresponding to maximum efficiency. (*A*) Vorticity field (red, positive; blue, negative) with velocity vectors shown as black arrows (*Upper*) and velocity magnitude shown in *Lower* (bright, high speed; dark, low speed). The snapshots correspond to $t = 26.12$, i.e., point $\eta_{max}(A)$ in Fig. 3*A*. Demarcations are shown at every 0.2*L* along the body center line for reference. The wake vortices intercepted by the follower (W_{1U}, W_{1L}, W_{2U}, W_{2L}), the lifted vortices created by interaction of the body with the flow (L_1, L_2, and L_3), and secondary vorticity S_1 generated by L_1 have been annotated. (*B*) Flow-induced force vectors (*Upper*) and body deformation velocity (*Lower*) at $t = 26.12$. (*C* and *D*) Deformation power (*C*) and thrust power (*D*) (with negative values indicating drag power) acting on the upper surface of follower. The red line indicates the average over 10 different snapshots ranging from $t = 30.12$ to $t = 39.12$. The envelope signifies the SD among the 10 snapshots. (*E* and *F*) Deformation power (*E*) and thrust power (*F*) on the lower (left lateral) surface of the swimmer.

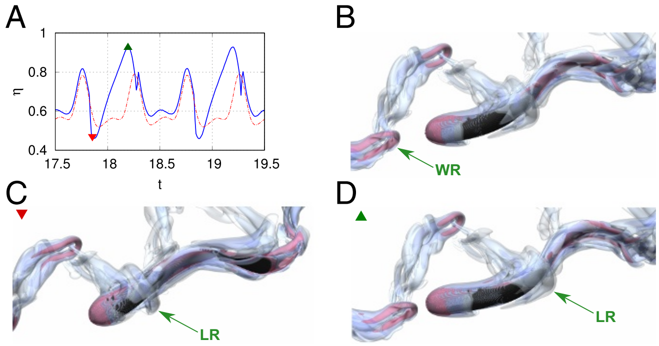

Fig. 5. The 3D swimmer interacting with WRs. (*A*) Swimming efficiency for a 3D leader (dash-dot red line) and a follower (solid blue line) that adjusts its undulations via a proportional-integrator (PI) feedback controller to maintain a specified position in the wake. After an initial transient, the patterns visible in the efficiency curves repeat periodically with T_p. Time instances where the follower attains its minimum and maximum swimming efficiency have been marked with an inverted red triangle and an upright green triangle, respectively. The sudden jumps at $t \approx 18.3$ and 19.3 correspond to adjustments made by the PI controller. (*B*) An oncoming WR is intercepted by the head of the follower and generates a new LR (*C*) similar to the 2D case (Fig. 4). As this ring interacts with the deforming body, it lowers the swimming efficiency initially ($t \approx 17.8$; *A* and *C*), but provides a noticeable benefit further downstream ($t \approx 18.2$; *A* and *D*).

relative velocity, for instance, near the high-velocity spot generated by vortex L_2 (Fig. 4). This dependence of swimming efficiency on a complex interplay between wake vortices and body deformation aligns closely with experimental findings (13, 27). We remark that the majority of the results presented here are obtained with a steadily swimming leader. However, with no additional training, IS_η is able to exploit the wake of a leader executing unfamiliar maneuvers, by deliberately choosing to interact with the unsteady wake, as seen in Movies S5 and S6. The smart follower is able to respond effectively to such unfamiliar situations, since it is exposed to a variety of perturbations while taking random actions during training. This observation demonstrates the robustness of the RL algorithm to uncertainties in the environment and further establishes its suitability for use in realistic scenarios.

Having examined the behavior and physical mechanisms associated with energy savings, we now formulate and test a simple control rule that enables efficient coordinated swimming. We remark that this is a combination of RL and DNSs in a reverse-engineering context, where: (*i*) We use the capability of RL to discern useful patterns from a large cache of simulation data; (*ii*) we analyze the physical aspects of the resulting optimal strategy, to identify the behavior and mechanisms that lead to energetic benefits, and finally; (*iii*) we use this understanding to devise a rule-based control algorithm for sustained energy-efficient synchronized swimming, in a notably more complex 3D setting. To the best of our knowledge, there is no work available in the literature that investigates the flow physics governing interactions among multiple independent swimmers, by using high-fidelity simulations of 3D NS equations.

Given the head-synchronization tendency of the 2D smart swimmer IS_η, we first identify suitable locations behind a 3D leader where the flow velocity would match a follower's head motion (*SI Appendix*, Fig. S7). A feedback controller is then used to regulate the undulations of two followers to maintain these target coordinates on either branch of the diverging wake, as shown in Fig. 1*B* and Movie S1. We note that a fish following in-line behind the leader would not benefit in the present 3D simulations, since the region behind the leader remains quiescent owing to the diverging wake. The controlled motion yields an 11% increase in average swimming efficiency for each of the followers (Fig. 5*A*) and a 5% reduction in each of their CoT. Overall, the group experiences a 7.4% increase in efficiency when compared with three isolated noninteracting swimmers. The mechanism of energy savings closely resembles that observed for the 2D swimmer; an oncoming WR (Fig. 5*B*) interacts with the deforming body to generate a "lifted-vortex" ring (LR; Fig. 5*C*). As this new ring proceeds along the length of the body, it modulates the follower's swimming efficiency as observed in Fig. 5. Remarkably, the positioning of the lifted ring at the instants of minimum and maximum swimming efficiency resembles the corresponding positioning of lifted vortices in the 2D case; a slight dip in efficiency corresponds to lifted vortices interacting with the anterior section of the body (Fig. 5*C* and *SI Appendix*, Fig. S5), whereas an increase occurs upon their interaction with the midsection (Figs. 4 and 5*D*).

These results showcase the capability of machine learning, and deep RL in particular, for discovering effective solutions to complex physical problems with inherent spatial and temporal nonlinearities, in a completely data-driven and model-free manner. Deep RL is especially useful in scenarios where decisions must be taken adaptively in response to a dynamically evolving environment, and the best control strategy may not be evident a priori due to unpredictable time delay between actions and their effect. This necessitates the use of recurrent networks capable of encoding time dependencies, which can have a demonstrable impact on the physical outcome, as shown in *SI Appendix*, Fig. S4. In conclusion, we demonstrate that deep RL can produce efficient navigation algorithms for use in complex flow fields, which in turn can be used to formulate control rules that are effective in decidedly more complex settings and thus have promising implications for energy savings in autonomous robotic swarms.

Methods

We perform 2D and 3D simulations of multiple self-propelled swimmers using wavelet adapted vortex methods to discretize the velocity–vorticity form of the NS equations (in 2D) and their velocity pressure form along with the pressure-projection method (in 3D) using finite differences on a uniform computational grid. The swimmers adapt their motion using deep RL. The learning process is greatly accelerated by using recurrent neural networks with long short-term memory as a surrogate of the value function for the smart swimmer. Details regarding the simulation methods and the RL algorithm are provided in *SI Appendix*.

ACKNOWLEDGMENTS. This work was supported by European Research Council Advanced Investigator Award 341117 and Swiss National Science Foundation Sinergia Award CRSII3 147675. Computational resources were provided by Swiss National Supercomputing Centre (CSCS) Project s658.

1. Schmidt J (1923) Breeding places and migrations of the Eel. *Nature* 111:51–54.
2. Lang TG, Pryor K (1966) Hydrodynamic performance of porpoises (*Stenella attenuata*). *Science* 152:531–533.
3. Aleyev YG (1977) Nekton (Springer, The Netherlands).
4. Triantafyllou MS, Weymouth GD, Miao J (2016) Biomimetic survival hydrodynamics and flow sensing. *Annu Rev Fluid Mech* 48:1–24.
5. Breder CM (1965) Vortices and fish schools. *Zool Sci Contrib N Y Zool Soc* 50:97–114.
6. Weihs D (1973) Hydromechanics of fish schooling. *Nature* 241:290–291.
7. Shaw E (1978) Schooling fishes: The school, a truly egalitarian form of organization in which all members of the group are alike in influence, offers substantial benefits to its participants. *Am Sci* 66:166–175.
8. Pavlov DS, Kasumyan AO (2000) Patterns and mechanisms of schooling behavior in fish: A review. *J Ichthyol* 40(Suppl 2):S163–S231.
9. Burgerhout E, et al. (2013) Schooling reduces energy consumption in swimming male European eels, *Anguilla anguilla* L. *J Exp Mar Biol Ecol* 448:66–71.

10. Whittlesey RW, Liska S, Dabiri JO (2010) Fish schooling as a basis for vertical axis wind turbine farm design. *Bioinspir Biomim* 5:035005.
11. Chapman JW, et al. (2011) Animal orientation strategies for movement in flows. *Curr Biol* 21:R861–R870.
12. Montgomery JC, Baker CF, Carton AG (1997) The lateral line can mediate rheotaxis in fish. *Nature* 389:960–963.
13. Liao JC, Beal DN, Lauder GV, Triantafyllou MS (2003) Fish exploiting vortices decrease muscle activity. *Science* 302:1566–1569.
14. Oteiza P, Odstrcil I, Lauder G, Portugues R, Engert F (2017) A novel mechanism for mechanosensory-based rheotaxis in larval zebrafish. *Nature* 547:445–448, and erratum (2017) 549:292.
15. Herskin J, Steffensen JF (1998) Energy savings in sea bass swimming in a school: Measurements of tail beat frequency and oxygen consumption at different swimming speeds. *J Fish Biol* 53:366–376.
16. Killen SS, Marras S, Steffensen JF, McKenzie DJ (2012) Aerobic capacity influences the spatial position of individuals within fish schools. *Proc Biol Sci* 279:357–364.
17. Ashraf I, et al. (2017) Simple phalanx pattern leads to energy saving in cohesive fish schooling. *Proc Natl Acad Sci USA* 114:9599–9604.
18. Pitcher TJ (1986) Functions of shoaling behaviour in teleosts. *The Behaviour of Teleost Fishes*, ed Pitcher TJ (Springer, Boston), pp 294–337.
19. Lopez U, Gautrais J, Couzin ID, Theraulaz G (2012) From behavioural analyses to models of collective motion in fish schools. *Interf Focus* 2:693–707.
20. Daghooghi M, Borazjani I (2015) The hydrodynamic advantages of synchronized swimming in a rectangular pattern. *Bioinspir Biomim* 10:056018.
21. Gazzola M, Hejazialhosseini B, Koumoutsakos P (2014) Reinforcement learning and wavelet adapted vortex methods for simulations of self-propelled swimmers. *SIAM J Sci Comput* 36:B622–B639.
22. Maertens AP, Gao A, Triantafyllou MS (2017) Optimal undulatory swimming for a single fish-like body and for a pair of interacting swimmers. *J Fluid Mech* 813:301–345.
23. Mnih V, et al. (2015) Human-level control through deep reinforcement learning. *Nature* 518:529–533.
24. Müller UK, Smit J, Stamhuis EJ, Videler JJ (2001) How the body contributes to the wake in undulatory fish swimming. *J Exp Biol* 204:2751–2762.
25. Kern S, Koumoutsakos P (2006) Simulations of optimized anguilliform swimming. *J Exp Biol* 209:4841–4857.
26. Borazjani I, Sotiropoulos F (2008) Numerical investigation of the hydrodynamics of carangiform swimming in the transitional and inertial flow regimes. *J Exp Biol* 211:1541–1558.
27. Liao JC, Beal DN, Lauder GV, Triantafyllou MS (2003) The Kármán gait: Novel body kinematics of rainbow trout swimming in a vortex street. *J Exp Biol* 206:1059–1073.
28. Hunt JCR, Wray AA, Moin P (1988) Eddies, streams, and convergence zones in turbulent flows. *Studying Turbulence Using Numerical Simulation Databases, 2. Report CTR-S88*, pp 193–208.
29. Sutton RS, Barto AG (1998) *Reinforcement Learning: An Introduction* (MIT Press, Cambridge, MA).
30. Gazzola M, Tchieu AA, Alexeev D, de Brauer A, Koumoutsakos P (2016) Learning to school in the presence of hydrodynamic interactions. *J Fluid Mech* 789:726–749.
31. Reddy G, Celani A, Sejnowski TJ, Vergassola M (2016) Learning to soar in turbulent environments. *Proc Natl Acad Sci USA* 113:E4877–E4884.
32. Colabrese S, Gustavsson K, Celani A, Biferale L (2017) Flow navigation by smart microswimmers via reinforcement learning. *Phys Rev Lett* 118: 158004.
33. Novati G, et al. (2017) Synchronisation through learning for two self-propelled swimmers. *Bioinspir Biomim* 12:036001.
34. Weihs D (1975) *Swimming and Flying in Nature*, eds Wu TYT, Brokaw CJ, Brennen C (Springer, Boston), Vol 2, pp 703–718.

PNAS
www.pnas.org

Supplementary Information for

Efficient collective swimming by harnessing vortices through deep reinforcement learning

Siddhartha Verma, Guido Novati, Petros Koumoutsakos

Petros Koumoutsakos.
E-mail: petros@ethz.ch

This PDF file includes:

Supplementary text
Figs. S1 to S10
Table S1
Captions for Movies S1 to S7
References for SI reference citations

Other supplementary materials for this manuscript include the following:

Movies S1 to S7

Supporting Information Text

Methods

Simulation details. The simulations presented here are based on the incompressible Navier-Stokes (NS) equations:

$$\nabla \cdot \mathbf{u} = 0$$
$$\frac{\partial \mathbf{u}}{\partial t} + \mathbf{u} \cdot \nabla \mathbf{u} = -\frac{\nabla P}{\rho_f} + \nu \nabla^2 \mathbf{u} + \lambda \chi (\mathbf{u}_s - \mathbf{u})$$

Each swimmer is represented on the computational grid via the characteristic function χ, and interacts with the fluid by means of the penalty[1] term $\lambda\chi\left(\mathbf{u}_s - \mathbf{u}\right)$. Here, $\mathbf{u}_s$ denotes the swimmer's combined translational, rotational, and deformation velocity, whereas $\mathbf{u}$ and ν correspond to the fluid velocity and viscosity, respectively. P represents the pressure, and the fluid density is denoted by ρ_f.

The vorticity form of the NS equations was used for the two-dimensional simulations, with $\lambda = 1e6$. A wavelet adaptive grid[2] with an effective resolution of 4096^2 points was used to discretize a unit square domain. A lower effective resolution of 1024^2 points was used for the training-simulations to minimize computational cost. We have determined in previous tests that this resolution provides a reasonable balance between speed and accuracy.[3] The pressure-Poisson equation ($\nabla^2 P = -\rho_f \left(\nabla \mathbf{u}^T : \nabla \mathbf{u}\right) + \rho_f \lambda \nabla \cdot \left(\chi \left(\mathbf{u}_s - \mathbf{u}\right)\right)$), necessary for estimating the distribution of flow-induced forces on the swimmers' bodies, was solved using the Fast Multipole Method with free-space boundary conditions.[3]

The three-dimensional simulations employed the pressure-projection method for solving the NS equations.[4] The simulations were parallelized via the CUBISM framework,[5] and used a uniform grid consisting of $2048 \times 1024 \times 256$ points in a domain of size $1 \times 0.5 \times 0.125$, with penalty parameter $\lambda = 1e5$. Further grid-refinement by $1.5\times$ in all three directions, and increasing the penalty parameter to $1e6$ resulted in no discernible change in the swimmer's speed. Thus, the lower grid resolution was selected to keep computational cost manageable. The CFL (Courant-Friedrichs-Lewy) number was constrained to be less than 0.1, resulting in approximately 2500 time steps per tail-beat period. The non-divergence-free deformation of the self-propelled swimmers was incorporated into the pressure-Poisson equation as follows:

$$\nabla^2 P = \frac{\rho_f}{\Delta t} \left(\nabla \cdot \mathbf{u}^\star - \chi \nabla \cdot \mathbf{u}_s\right), \quad [1]$$

where $\mathbf{u}^\star$ represents the intermediate velocity from the convection-diffusion-penalization fractional steps. Equation 1 was solved using a distributed Fast Fourier Transform library (AccFFT[6]). To prevent a periodic recycling of the outflow, the velocity field was smoothly truncated to zero as it approached the outflow boundary. We ensured that periodicity and velocity smoothing do not impact the results presented, by running simulations with a domain enlarged in all three spatial directions.

Flow-induced forces, and energetics variables. The pressure-induced and viscous forces acting on the swimmers are computed as follows:[3]

$$\mathbf{dF}_P = -P\mathbf{n}\, dS \quad [2]$$
$$\mathbf{dF}_\nu = 2\mu \mathbf{D} \cdot \mathbf{n}\, dS \quad [3]$$

Here, P represents the pressure acting on the swimmer's surface, $\mathbf{D} = \left(\nabla \mathbf{u} + \nabla \mathbf{u}^T\right)/2$ is the strain-rate tensor on the surface, and dS denotes the infinitesimal surface area. Since self-propelled swimmers generate zero net average thrust (and drag) during steady swimming, we determine the instantaneous thrust as follows:

$$\text{Thrust} = \frac{1}{2\|\mathbf{u}\|} \iint \left(\mathbf{u} \cdot \mathbf{dF} + |\mathbf{u} \cdot \mathbf{dF}|\right), \quad [4]$$

where $\mathbf{dF} = \mathbf{dF}_P + \mathbf{dF}_\nu$. Similarly, the instantaneous drag may be determined as:

$$\text{Drag} = \frac{1}{2\|\mathbf{u}\|} \iint \left(\mathbf{u} \cdot \mathbf{dF} - |\mathbf{u} \cdot \mathbf{dF}|\right) \quad [5]$$

Using these quantities, the thrust-, drag-, and deformation-power are computed as:

$$P_{Thrust} = \text{Thrust} \cdot \|\mathbf{u}\| \quad [6]$$
$$P_{Drag} = -\text{Drag} \cdot \|\mathbf{u}\| \quad [7]$$
$$P_{Def} = -\iint \mathbf{u}_{Def} \cdot \mathbf{dF} \quad [8]$$

where $\mathbf{u}_{Def}$ represents the deformation-velocity of the swimmer's body. The double-integrals in these equations represent surface-integration over the swimmer's body, and yield measurements for time-series analysis. On the other hand, only the integrand is evaluated when surface-distributions of thrust-, drag-, or deformation-power are required (as in main Figs. 4c to 4f).

The instantaneous swimming-efficiency is based on a modified form of the Froude efficiency proposed in ref.:[7]

$$\eta = \frac{P_{Thrust}}{P_{Thrust} + \max(P_{Def}, 0)} \quad [9]$$

To compute both η and the Cost of Transport (CoT), we neglect negative values of P_{Def}, which can result from beneficial interactions of the smart-swimmer with the leader's wake:

$$CoT(t) = \frac{\int_{t-T_p}^{t} \max(P_{Def}, 0) dt}{\int_{t-T_p}^{t} \|\mathbf{u}\| dt} \quad [10]$$

This restriction accounts for the fact that the elastically rigid swimmer may not store energy furnished by the flow, and yields a conservative estimate of potential savings in the CoT. We note that percentage-changes in P_{Def}, reported in the main text and the supplementary section, have been computed using this bounded value to avoid overstating any potential benefits.

Swimmer shape and kinematics. The Reynolds number of the self-propelled swimmers is computed as $Re = L^2/(\nu T_p)$. The body-geometry is based on a simplified model of a zebrafish.[8] The half-width of the 2D profile is described as follows:

$$w(s) = \begin{cases} \sqrt{2w_h s - s^2} & 0 \le s < s_b \\ w_h - (w_h - w_t)\left(\dfrac{s - s_b}{s_t - s_b}\right) & s_b \le s < s_t \\ w_t \dfrac{L - s}{L - s_t} & s_t \le s \le L \end{cases} \quad [11]$$

where s is the arc-length along the midline of the geometry, $L = 0.1$ is the body length, $w_h = s_b = 0.04L$, $s_t = 0.95L$, and $w_t = 0.01L$. For 3D simulations, the geometry is comprised of elliptical cross sections, with the half-width $w(s)$ and half-height $h(s)$ described via cubic B-splines.[8] Six control-points define the half-width: $(s/L, w/L) = [(0.0, 0.0),\ (0.0, 0.089),\ (1/3, 0.017),\ (2/3, 0.016),\ (1.0, 0.013),\ (1.0, 0.0)]$; whereas eight control-points define the half-height: $(s/L, h/L) = [(0.0, 0.0),\ (0.0, 0.055),\ (0.2, 0.068),\ (0.4, 0.076),\ (0.6, 0.064),\ (0.8, 0.0072),\ (1.0, 0.11),\ (1.0, 0.0)]$. The length was set to $L = 0.2$, which keeps the grid-resolution, i.e., the number of points along the fish midline, comparable to the 2D simulations. Body-undulations for both 2D and 3D simulations were generated as a travelling-wave defining the curvature along the midline:

$$k(s,t) = A(s)\sin\left(\frac{2\pi t}{T_p} - \frac{2\pi s}{L}\right) \quad [12]$$

Here $A(s)$ is the curvature amplitude and varies linearly from $A(0) = 0.82$ to $A(L) = 5.7$.

Reinforcement Learning. Reinforcement learning (RL)[9] is a process by which an agent (in this case, the smart-swimmer) learns to earn rewards through trial-and-error interaction with its environment. At each turn, the agent observes the state of the environment s_n and performs an action a_n, which influences both the transition to the next state s_{n+1} and the reward received r_{n+1}. The agent's goal is to learn the optimal control policy $a_n = \pi^*(s_n)$ which maximises the action value $Q^*(s_n, a_n)$, defined as the sum of discounted future rewards:

$$Q^*(s_n, a_n) = \max_\pi \mathbb{E}\left(r_{n+1} + \gamma r_{n+2} + \gamma^2 r_{n+3} + \ldots \,|\, a_m = \pi(s_m)\ \forall m \in [n+1, \mathcal{T}]\right) \quad [13]$$

Here, $\mathcal{T}$ denotes the terminal state of a training-simulation, and the discount factor γ is set to 0.9. The optimal action-value function $Q^*(s_n, a_n)$ is a fixed point of the Bellman equation: $Q^*(s_n, a_n) = \mathbb{E}\left[r_{n+1} + \gamma \max_{a'} Q^*(s_{n+1}, a')\right]$.[10] We approximate $Q^*(s_n, a_n)$ using a neural network[11] with weights w_k, which are updated iteratively to minimize the temporal difference error:

$$\text{TD}_{\text{err}} = \mathbb{E}_{s_n, a_n, s_{n+1}}\left[r_{n+1} + \gamma Q(s_{n+1}, a'; \mathrm{w}_-) - Q(s_n, a_n; \mathrm{w}_k)\right] \quad [14]$$

Here, w_- is a set of target weights, and a' is the best action in state s_{n+1} computed with the current weights ($a' = \arg\max_a Q(s_{n+1}, a; \mathrm{w}_k)$). The target weights w_- are updated towards the current weights as $\mathrm{w}_- \leftarrow (1-\alpha)\mathrm{w}_- + \alpha \mathrm{w}_k$, where $\alpha = 10^{-4}$ is an under-relaxation factor used to stabilize the algorithm.[11]

States and actions. The six observed-state variables perceived by the learning agent include Δx, Δy, θ, the two most recent actions taken by the agent, and the current tail-beat 'stage' $\mathrm{mod}(t, T_p)/T_p$. The permissible range of the observed-state variables is limited to: $1 \le \Delta x/L \le 3$; $|\Delta y|/L \le 1$ (boundary depicted by R_{end} in SI Appendix Fig. S8); and $|\theta| \le \pi/2$. If the agent exceeds any of these thresholds, the training-simulation terminates and the agent receives a terminal reward $R_{end} = -1$.

The smart-swimmer (or agent) is capable of manoeuvering by actively manipulating the curvature-wave travelling down the body. This is accomplished by linearly superimposing a piecewise function on the baseline curvature $k(s,t)$ (equation 12):

$$k_{\text{Agent}}(s,t) = k(s,t) + A(s) M(t, T_p, s, L) \quad [15]$$

The curve $M(t, T_p, s, L)$ is composed of 3 distinct segments:

$$M(t, T_p, s, L) = \sum_{j=0}^{2} b_{n-j} \cdot m\left(\frac{t - t_{n-j}}{T_p} - \frac{s}{L}\right) \quad [16]$$

The curve m is a clamped cubic spline with $m(0) = m'(0) = 0$, $m(1/2) = m'(1/2) = 0$, and $m(1/4) = 1$, $m'(1/4) = 0$. t_n represents the time-instance when action a_n is taken, whereas b_n represents the corresponding control-amplitude, which may take five discrete values: 0, ± 0.25, and ± 0.5.

Neural network architecture. One of the assumptions in RL is that the transition probability to a new state s_{n+1} is independent of the previous transitions, given s_n and a_n, i.e.,:

$$p(s_{n+1} \,|\, s_n, a_n) = p(s_{n+1} \,|\, s_n, a_n, \ldots, s_0, a_0) \quad [17]$$

This assumption is invalidated whenever the agent has a limited perception of the environment. In most realistic cases the agent receives an observation o_n rather than the complete state of the environment s_n. Therefore, past observations carry information relevant for future transitions (i.e., $p(o_{n+1} \,|\, o_n, a_n) \ne p(o_{n+1} \,|\, o_n, a_n, \ldots, o_0, a_0)$), and should be taken into account in order to make optimal decisions. This operation can be approximated by a Recurrent Neural Network (RNN), which can learn to compute and remember important features in past observations. In this work we approximate the action-value function with a LSTM-RNN[12] composed of three layers of 24 fully connected LSTM cells each, and terminating in a linear layer (SI Appendix Fig. S3). The last layer computes a vector of action-values $\mathbf{q}_n = Q(o_n; y_{n-1}, \mathrm{w}_k)$ with one component $q_n^{(a)}$ for each possible action a available to the agent (y_{n-1} represents the activation of the network at the previous turn).

Training procedure. During training, both the leader and the follower (learning agent) start from rest. The leader swims steadily along a straight line, whereas the follower manoeuvers according to the actions supplied to it. Multiple independent simulations run simultaneously, with each of these sending the current observed-state o_n of the agent to a central processor, and in turn receiving the next action a_n to be performed. The central processor computes a_n using an ϵ-greedy policy (with ϵ gradually annealed from 1 to 0.1) from the most recently updated Q function. Once a training-simulation reaches a terminal state (e.g., the follower hits the boundary labelled R_{end} in SI Appendix Fig. S8), all the messages exchanged between the simulation and the central processor are appended to a training set of sequences $\mathcal{R}$. In the meantime, the network is continually updated by sampling B sequences from the set $\mathcal{R}$, according to algorithm 1. The batch gradient g is computed with back propagation through time (BPTT).[14] The network weights are then updated with the Adam stochastic optimization algorithm.[13]

Algorithm 1: Asynchronous recurrent DQN algorithm.

```
initialize network w_0 and target network w_- = w_0;
initialize set of transition sequences R = ∅;
repeat
    N ← 0;
    sample batch of B sequences from R;
    for sequence j ∈ [1, ..., B] do
        [q_{j,0}, y_{j,0}] = Q(o_{j,0}; ∅, w_k);
        for turns n ∈ [0, ..., T_j − 1] do
            [q_{j,n+1}, y_{j,n+1}] = Q(o_{j,n+1}; y_{j,n}, w_k);
            [q̃_{j,n+1}, ỹ_{j,n+1}] = Q(o_{j,n+1}; y_{j,n}, w_-);
            a' = arg max_a [q^{(a)}_{j,n+1}];
            if s_{j,n+1} is terminal then
                e_{j,n} = r_{j,n+1} − q^{(a_n)}_{j,n};
            else
                e_{j,n} = r_{j,n+1} + γ q̃^{(a')}_{j,n+1} − q^{(a_n)}_{j,n};
            end
            N ← N + 1;
        end
    end
    perform BPTT: g = (1/N) Σ_j Σ_n e_{j,n} ∇_w q^{(a_n)}_{j,n};
    update weights w_{k+1} by passing g to the Adam algorithm[13];
    update target network: w_- ← (1 − α)w_- + α w_{k+1};
    k ← k + 1;
until Q(o, a; w_k) = Q*(o, a);
```

A total of 1200 forward simulations were used during the training procedure, which corresponds to approximately 46000 transitions (action-decisions) by the learning agent. To determine the convergence of network-fitting, we inspected the histogram distribution of the follower's preferred Δx position (similar to main Fig. 2e) during the final and the penultimate 10000 transitions. We observed that the distribution did not change noticeably towards the end of training, which indicates that the RL algorithm has arrived close to a local minimum. Running additional simulations would not alter the histogram distribution appreciably, and any incremental improvements would incur too large a computational cost to be justifiable.

Proportional-Integral feedback controller. The PI controller modulates the 3D follower's body-kinematics, which allows it to maintain a specific position (x_{tgt}, y_{tgt}, z_{tgt}) relative to the leader:

$$k(s,t) = \alpha(t)A(s)\left[\sin\left(\frac{2\pi t}{T_p} - \frac{2\pi s}{L}\right) + \beta(t)\right] \quad [18]$$

The factor $\alpha(t)$ modifies the undulation envelope, and controls the acceleration or deceleration of the follower based on its streamwise distance from the target position:

$$\alpha(t) = 1 + f_1\left(\frac{x - x_{tgt}}{L}\right) \quad [19]$$

The term $\beta(t)$ adds a baseline curvature to the follower's midline to correct for lateral deviations:

$$\beta(t) = \frac{y_{tgt} - y}{L}\ (f_2|\theta| + f_3|\hat{\theta}|) \quad [20]$$

Here, θ represents the follower's yaw angle about the z-axis, and $\hat{\theta}$ is its exponential moving average: $\hat{\theta}_{t+1} = \frac{1-\Delta t}{T_p}\hat{\theta}_t + \frac{\Delta t}{T_p}\theta$. The swimmers' z-positions remain fixed at z_{tgt}, as out-of-plane motion is not permitted. The controller-coefficients were selected to have a minimal impact on regular swimming kinematics, which allows for a direct comparison of the follower's efficiency to that of the leader:

$$f_1 = 1 \quad [21]$$

$$f_2 = \max(0, 50\ \mathrm{sign}(\theta \cdot (y_{tgt} - y))) \quad [22]$$

$$f_3 = \max(0, 20\ \mathrm{sign}(\hat{\theta} \cdot (y_{tgt} - y))) \quad [23]$$

Supplementary Text, Figures, Tables, and Movies

Body-deformation during autonomous manoeuvres. The extent of body-bending that swimmers IS_η and IS_d undergo when manoeuvring is compared quantitatively in SI Appendix Fig. S1. A qualitative comparison was presented in main Fig. 2f. We observe that the body-deformation of IS_d is noticeably higher than that of a steady swimmer (with relative curvature 1), which implies a tendency to take aggressive turns. The deformation for swimmer IS_η is markedly lower, which plays an instrumental role in reducing the power required for undulating the body against flow-induced forces.

Comparison of four different swimmers. The performance metrics for four different swimmers are compared in SI Appendix Fig. S2. Interacting swimmer IS_d occasionally attains higher speed than IS_η (SI Appendix Fig. S2a), but at the cost of much higher energy expenditure (SI Appendix Fig. S2c and Table S1). Moreover, the speeds of solitary swimmers SS_η and SS_d are lower than those of either interacting swimmer (IS_η and IS_d), which suggests that wake-interactions may benefit a follower in some aspects, regardless of the goal being pursued. However, we stress that while interacting with a leader's wake appropriately may yield a benefit compared to the energy requirements of a steady solitary swimmer (e.g., IS_η - SI Appendix Fig. S2c), this may not be the case if the reinforcement learning reward does not account for energy usage. Both swimmers IS_d and SS_d have higher energetic costs of swimming compared to a steady solitary fish (Fig. S2c), which demonstrates that following a leader indiscriminately can indeed be disadvantageous. In SI Appendix Fig. S2d, P_{Def} attains negative values only for IS_η, which is indicative of maximum benefit extracted from flow-induced forces. Both IS_d and SS_d are capable of generating significantly higher thrust-power than IS_η, but suffer from larger deformation-power, and consequently, lower swimming-efficiency. Comparing the columns for IS_η and SS_η in Table S1, we note that interacting with a preceding wake has a measurable impact on swimming-performance; IS_η is approximately 32% more efficient than SS_η, spends 36% less energy per unit distance travelled, requires 29% less power for body-undulations, and generates 52% higher thrust-power. Wake-interactions may yield certain benefits even for the swimmer actively minimizing lateral displacement from the leader, primarily by increasing thrust-power, but at the penalty of higher energetic-cost for body-deformation, as can be surmised by comparing the data for IS_d and SS_d in SI Appendix Table S1. This observation further confirms that interacting with unsteady wakes may not prove to be beneficial overall, if the swimming-kinematics do not account for energetic considerations.

Uncovering underlying time-dependencies. While it is relatively straightforward to maintain a particular tandem formation via feedback control (when the follower strays too far to one side, a feedback controller can relay instructions to veer in the opposite direction), the same is not true for maximizing swimming-efficiency. It is difficult to formulate a simple set of a-priori rules for maximizing efficiency, especially in dynamically evolving conditions. This happens because: 1) the swimmer perceives only a limited representation of its environment (main Fig. 2a); and 2) there may be measurable delay between an action and its impact on the reward received over the long term. These traits make deep RL ideal for determining the optimal policy when maximizing swimming-efficiency, especially when augmented with recurrent neural networks (SI Appendix Fig. S3). These network architectures are adept at discovering and exploiting long-term time-dependencies. We remark that neither standard optimisation, nor optimal control[10] techniques are suitable for use in the current problem, both due to the need for adaptive control, and due to the unavailability of simplified sets of equations describing the system's response. Moreover, optimal-control algorithms evaluate multiple forward simulations at every decision-making step, which is decidedly impractical in the current study given the large computational cost of the forward Navier-Stokes simulations.

The advantage of using a Recurrent Neural Network (RNN). To illustrate the advantage of using a deep recurrent network, we compare the performance of a smart-swimmer trained to minimize lateral deviations (Δy) from a leader using two distinct neural network architectures: a Feedforward Neural Network (FNN) similar to the one used in our previous study;[15] and the more sophisticated deep Recurrent Neural Network (RNN) shown in Fig. S3. Using SI Appendix Fig. S4a, we observe that the FNN-trained smart-follower is unable to achieve its goal of maintaining $\Delta y = 0$ as rigorously as the RNN-trained follower, which clearly demonstrates the superior capability of the RNN. Moreover, in its attempt to maintain $\Delta y = 0$ rigorously, the RNN-trained swimmer executes severe turns (main Fig. 2f), which lead to an increase in its energy consumption (higher CoT in Fig. S4b). To explain the comparative energetic benefit observed by the FNN-trained swimmer (even though its reward does not account for energetic considerations), we note that it almost always settles close to the 'attractor point' $\Delta x = 2.2L$, where the head-motion is synchronised well with the wake flow. This leads to energetic gains for the FNN-based swimmer, although its primary objective of maintaining $\Delta y = 0$ is not achieved satisfactorily. We remark that similar migrations of a follower toward the favourable attractor point are observed, even when employing a feedback controller to attempt to hold position at an unfavourable location in the wake. We speculate that this may portend the existence of stability points throughout schooling formations, where minimal control-effort may yield large energetic gains.

Flow-interactions at the instant of minimum swimming-efficiency. The instant when swimmer IS_η attains the lowest efficiency during each half-period ($\eta_{min}(D)$ in main Fig. 3a) is examined in SI Appendix Fig. S5. The mean P_{Def} curve is mostly positive on both the lower and upper surfaces, with large positive peaks generated by interaction with the wake- and lifted-vortices. This increase in effort is not offset sufficiently by an increase in P_{Thrust}, resulting in low swimming-efficiency. Compared to the instance of maximum efficiency (main Fig. 4), increased effort is required in the head region, along with an increase in thrust-production by the tail section $s > 0.7L$.

Slight deviations impact performance. To examine the impact of small deviations in IS_η's trajectory on its performance, we compare two different time-instances (at the same tail-beat stage) in SI Appendix Fig. S6. At $t \approx 26.5$, IS_η deviates slightly to the left of its steady trajectory (Supplementary Movie S7), which throws it out of synchronization with the oncoming wake-vortices. The resulting reduction in efficiency at $t \approx 27.5$ indicates that even slight deviations are capable of impacting performance, and that there may be a measurable delay between actions and consequences. However, the smart-swimmer autonomously corrects for such deviations, and is able to quickly recover its optimal behaviour.

Correlation with the flow-field. The correlation-coefficient curve shown in main Fig. 2e, and the correlation map shown in SI Appendix Fig. S7, were computed as follows:

$$\rho(\mathbf{u}, \mathbf{u}_{\text{head}}) = \frac{\text{cov}\left(\mathbf{u}(x,y), \mathbf{u}_{head}\right)}{\sigma_{\mathbf{u}(x,y)}\ \sigma_{\mathbf{u}_{\text{head}}}} = \frac{\sum_t \mathbf{u}(x,y,t)\cdot\mathbf{u}_{\text{head}}(t)}{\sqrt{\sum_t \|\mathbf{u}(x,y,t)\|^2}\sqrt{\sum_t \|\mathbf{u}_{\text{head}}(t)\|^2}} \quad [24]$$

Here, $\mathbf{u}(x, y, t)$ was recorded in the wake of a solitary swimmer, whereas $\mathbf{u}_{\text{head}}(t)$ was recorded at the swimmer's head. Maxima in $\rho(\mathbf{u}, \mathbf{u}_{\text{head}})$ provide an estimate for the coordinates where a follower's head-movements would exhibit long-term synchronization with an undisturbed wake.

Limiting the exploration space. During training, the range of values that a smart-follower's states can take are constrained, as mentioned previously. This prevents excessive exploration of regions that involve no wake-interactions, and helps to minimize the computational cost of training-simulations. The limits of the bounding box (shown in SI Appendix Fig. S8) are kept sufficiently large to provide the follower ample room to swim clear of the unsteady wake, if it determines that interacting with the wake is unfavourable.

Power distribution in the presence/absence of a preceding wake. To determine the extent to which wake-induced interactions alter the distribution of P_{Def} and P_{Thrust}, both of which influence overall swimming-efficiency, we compare these quantities for IS_η and SS_η in SI Appendix Fig. S9. A similar comparison for IS_d and SS_d is shown in SI Appendix Fig. S10. For IS_η, a greater variation in P_{Def} and P_{Thrust} is observed (broad envelopes in SI Appendix Figs. S9a and S9b), compared to the solitary swimmer SS_η (SI Appendix Figs. S9c and S9d). This is caused by IS_η's interactions with the unsteady wake, which is absent for SS_η. The average P_{Def} for IS_η shows distinct negative troughs near the head ($s/L < 0.2$, SI Appendix Fig. S9a) and at $s/L = 0.6$. A lack of similar troughs for SS_η (SI Appendix Fig. S9c) implies that these benefits originate exclusively from wake-induced interactions. There is no apparent difference in drag for both IS_η and SS_η in the pressure-dominated region close to the head ($s \approx 0$). However, wake-induced interactions provide a pronounced increase in thrust-power generated by the midsection for IS_η (compare SI Appendix Figs. S9b and S9d, $0.2 < s/L < 0.4$). Among all of the four swimmers compared, only IS_η shows a distinct negative P_{Def} region close to the head ($s < 0.2L$), which further supports the occurrence of head-motion synchronization with flow-induced forces, when efficiency is maximized. Comparing the deformation- and thrust-power distribution for IS_d and SS_d in SI Appendix Fig. S10 provides additional evidence that wake-interactions have a marked impact on swimming-energetics.

Performance of IS_η with respect to an optimal solitary swimmer. A natural question (credited to one Referee) is whether solitary swimming may be preferred to swimming in the wake of a leader. The scenario of a solitary swimmer is an inherent part of the RL training procedure. There are no positional constraints imposed on the smart-follower during training, so it has the possibility to swim at a large lateral distance from the leader, free of the wake's influence and effectively as a solitary swimmer. If solitary swimming with optimal kinematics were preferable to interacting with the leader's wake, the RL algorithm would have converged to this swimming mode as the final strategy for IS_η, instead of preferring to harness the wake-vortices. We emphasize that RL cannot guarantee global minima, but during the training process we did not find solitary swimming as a preferred strategy, instead of the behaviour reported in the manuscript.

We note that optimal morphokinematics of solitary swimmers (albeit at $Re = 500$ and not $Re = 5000$ as studied herein) have been performed in our earlier work.[16] In principle one could train also an efficient solitary swimmer through Reinforcement Learning, but this will require changing the observed states. Finally one may remark that we could have used as baseline leader a swimmer that had been previously optimized. In this context, we have also conducted a parametric search to find the best steady-swimming kinematics for the present baseline fish model. The wake of optimal swimmers is not drastically different from the wake of the present swimmer, and it contains vortex rings that we believe the follower would have reacted to in similar fashion as to the present leader.

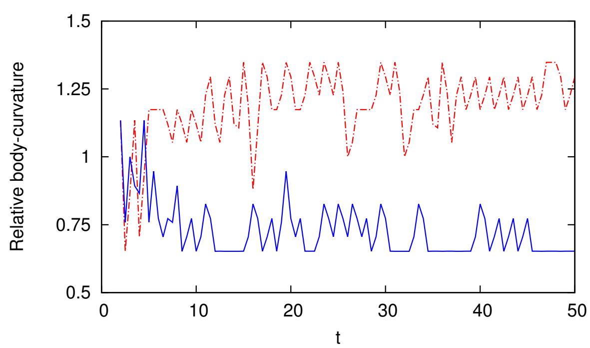

Fig. S1. Midline curvature. Severity of body-deformation for the swimmers IS_η (solid blue line) and IS_d (dash-dot red line), shown for 50 tail-beat periods starting from rest. The relative body-curvature is computed as $\Sigma_{i=1}^{6}|\kappa_i|$, normalized with the same metric for a solitary swimmer executing steady motion (κ_i represents the curvature at 6 control points along a swimmer's body).

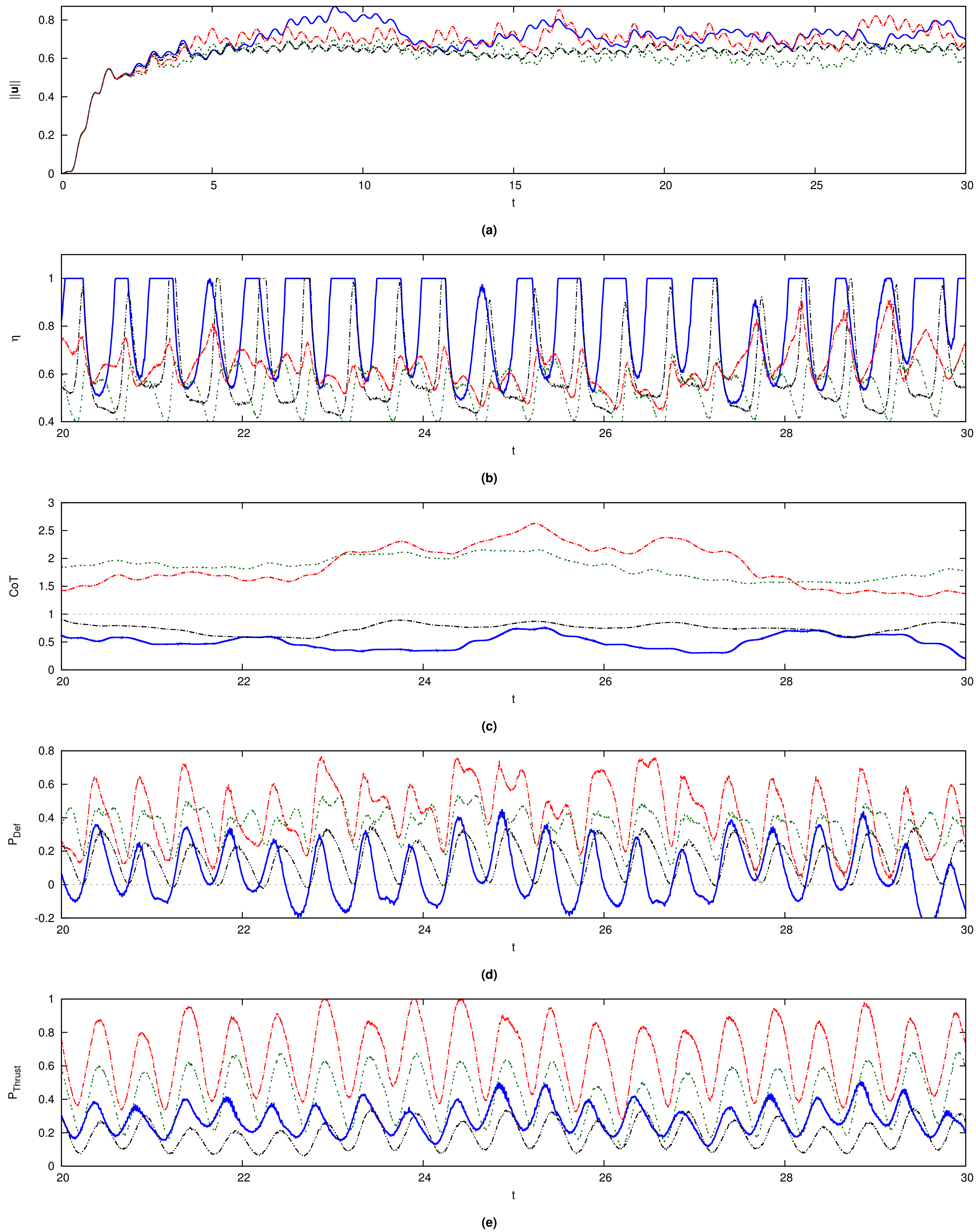

Fig. S2. Performance metrics for four different swimmers. Plots comparing (a) speed, (b) η, (c) CoT, (d) deformation-power , and (e) thrust-power for four different swimmers. The solid blue line corresponds to swimmer IS_{η}, the dash-double-dot black line to swimmer SS_{η} (a solitary swimmer executing actions identical to IS_{η}), the dash-dot red line to swimmer IS_{d}, and the double-dot green line to swimmer SS_{d} (a solitary swimmer executing actions identical to IS_{d}). The horizontal dashed line at $CoT = 1$ in (c) corresponds to a free-swimming solitary swimmer.

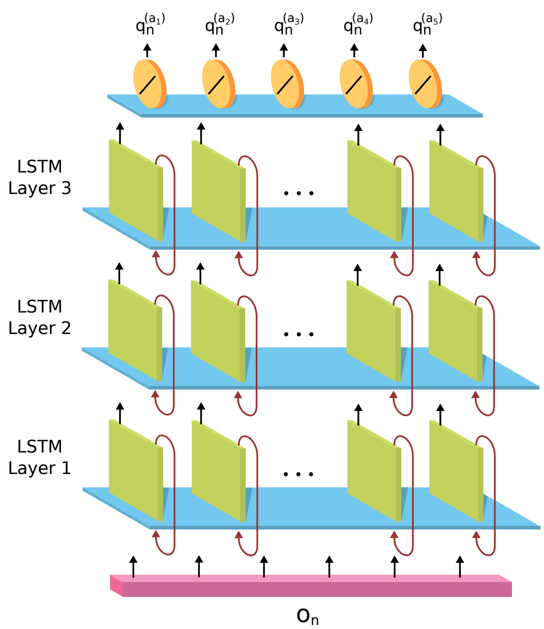

Fig. S3. Schematic of the Recurrent Neural Network (RNN). The RNN used in this study is composed of 3 LSTM layers, consisting of 24 cells (green blocks) each. The input layer (pink block) of the network comprises the 6 observed-state variables. The black arrows between different layers indicate all-to-all connections. The purple arrows indicate recurrent connections within each LSTM layer. The last layer consists of 5 output neurons (orange) with linear activation.

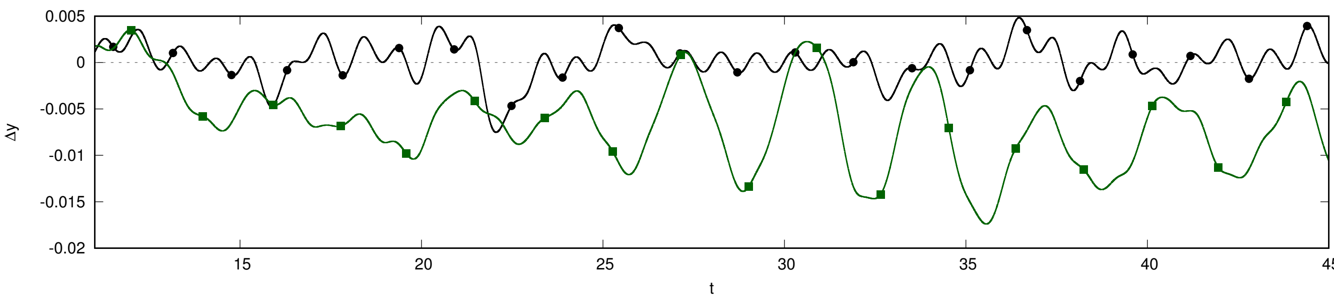

(a)

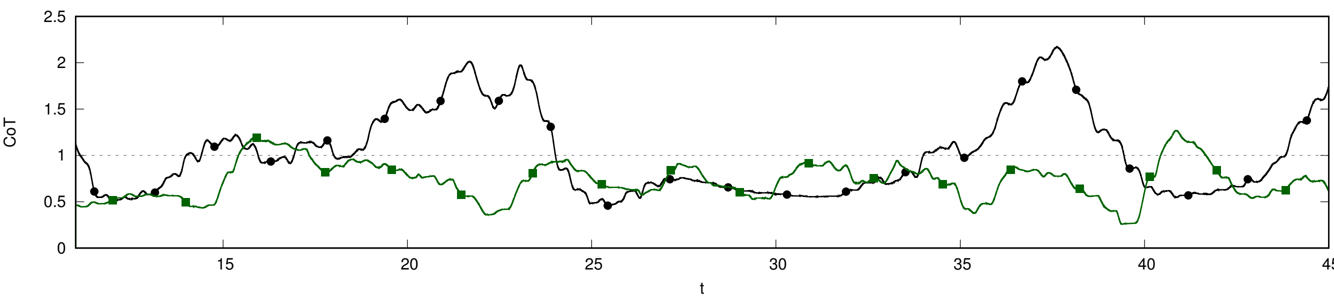

(b)

Fig. S4. Comparison of feedforward and recurrent neural networks. (a) Comparing the in-line following capability of smart-swimmers trained using a feedforward neural network (green line with square symbols), and the deep recurrent network shown in Fig. S3 (black line with circle symbols). The horizontal dashed line at $\Delta y = 0$ denotes the target specified for both smart-swimmers. (b) Cost of transport for the two swimmers. The horizontal dashed line at $CoT = 1$ corresponds to a free-swimming solitary swimmer.

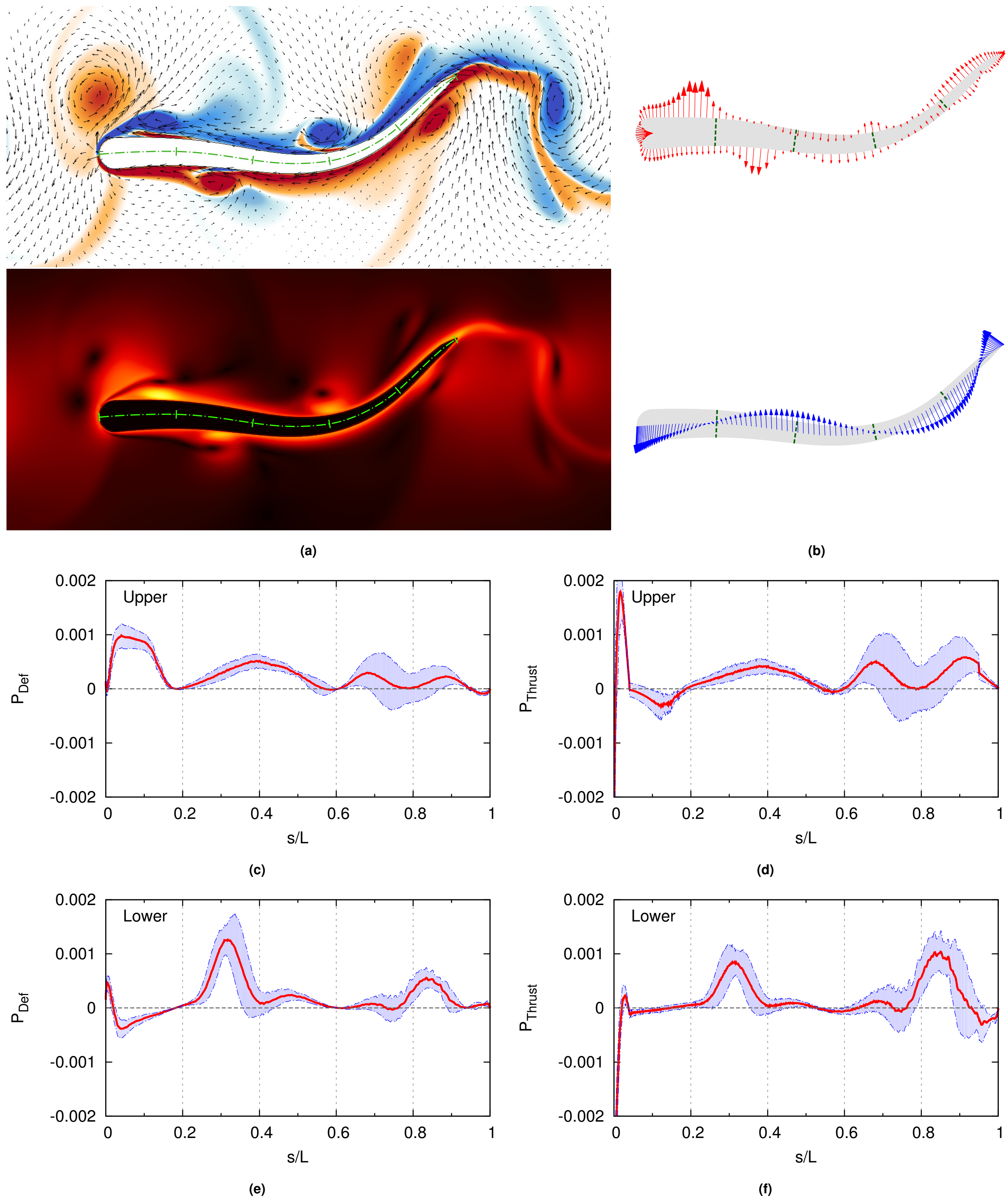

Fig. S5. Flow-field and flow-induced forces for IS_η, corresponding to minimum efficiency. (a) Vorticity field with the velocity vectors shown (top), and velocity magnitude (bottom) at $t = 26.87$ (point $\eta_{min}(D)$ in main Fig. 3). (b) Flow-induced force-vectors (top) and body-deformation velocity (bottom) at this instance. (c,d) Deformation-power and thrust-power acting on the upper (right lateral) surface of follower. The red line indicates the average over 10 different snapshots ranging from $t = 30.87$ to $t = 39.87$. The envelope denotes the standard deviation among the 10 snapshots. (e,f) Deformation-power and thrust-power on the lower (left lateral) surface of the fish.

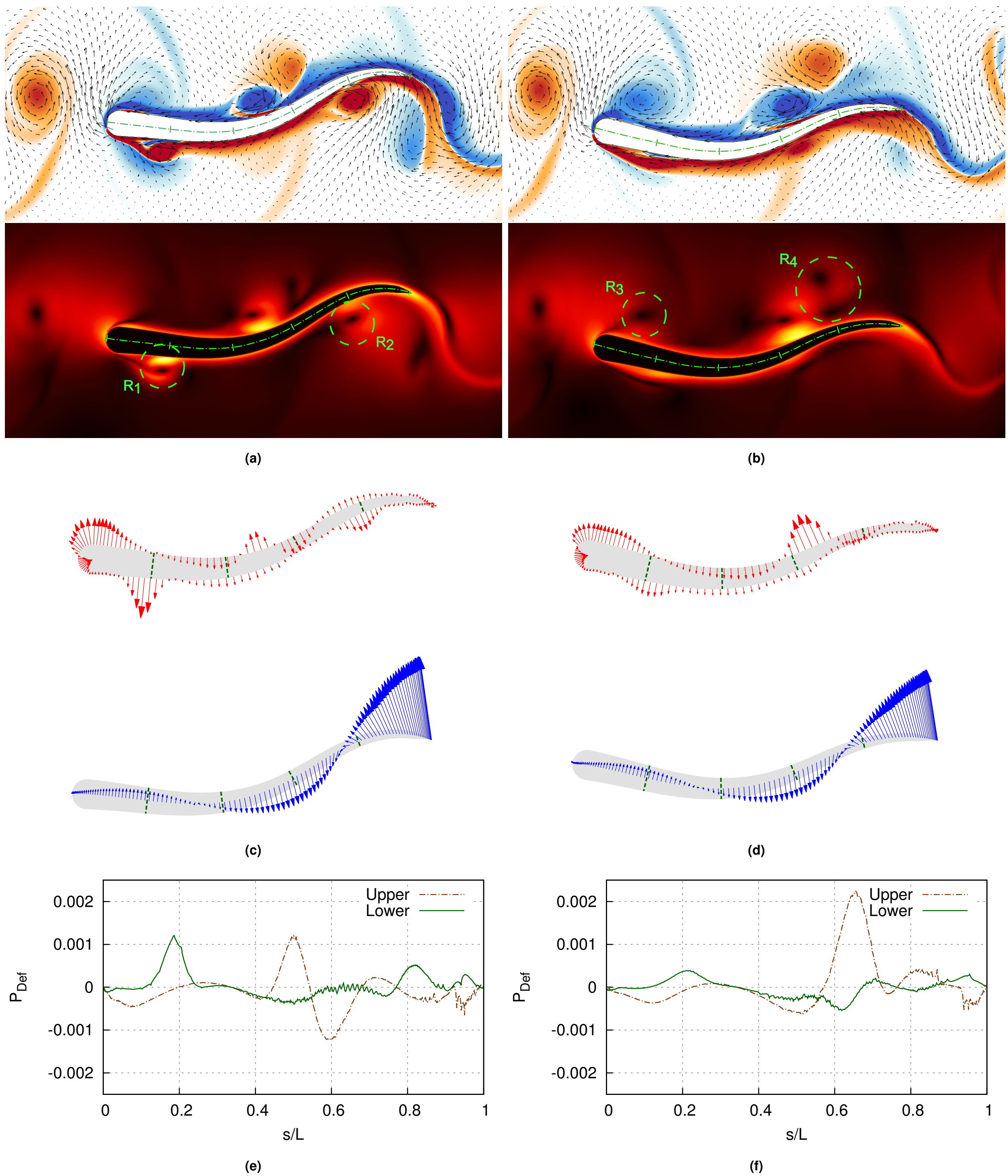

Fig. S6. Deviations impact performance. Comparison of two instances when a maximum in the swimming-efficiency is expected. The deformed shape and deformation-velocity for the two instances are similar, but differences in the flow-field influence efficiency. Panels on the left hand side of the page show data for IS_η at $t \approx 33.7$ ($\eta = 1$), whereas those on the right hand side correspond to $t \approx 27.7$ ($\eta = 0.86$). (a, b) Vorticity, velocity vectors, and velocity magnitude at the two time instances. A slight deviation in the follower's approach to the wake causes a noticeable change in the surrounding vortices, as well as in the velocity induced near the surface. The regions highlighting differences have been marked as R_1, R_2, R_3, and R_4. (c, d) A comparison of the surface force-vectors and body-deformation velocity. (e,f) There are notable differences in the distribution of P_{Def} on the upper and lower surfaces.

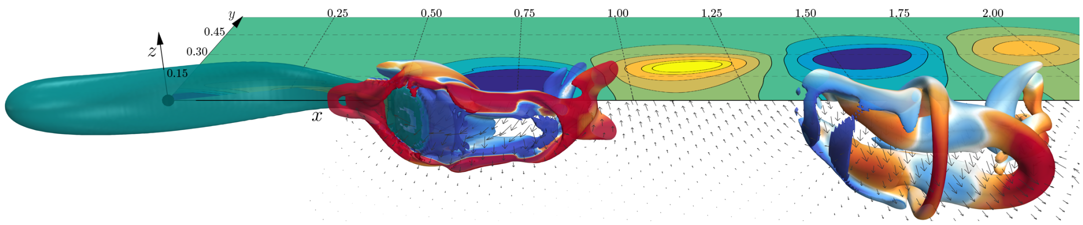

Fig. S7. Correlation map. The horizontal plane on the right side of the swimmer depicts the correlation-coefficient described by Equation 24. Areas of high correlation are denoted as yellow regions, whereas those of low correlation are shown in blue. The vortex rings shed are shown on the swimmer's left side, along with the velocity vectors on the left horizontal plane.

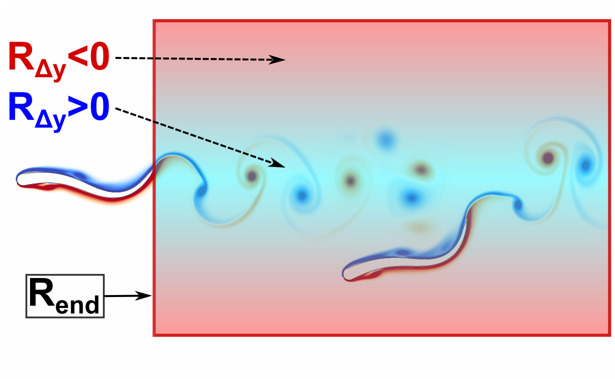

Fig. S8. Reward for IS_d. Visual representation of reward assigned to smart-swimmer IS_d, whose goal is to minimize its lateral displacement from the leader.

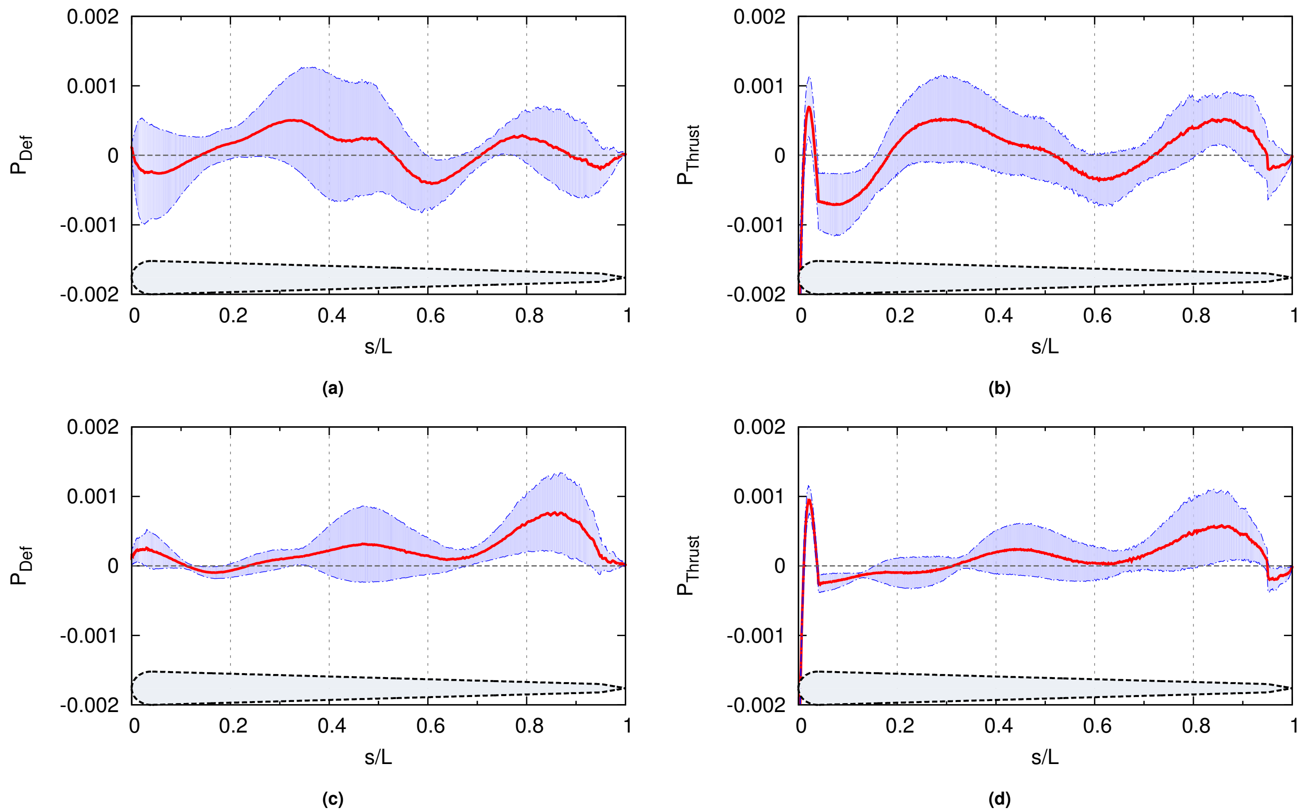

Fig. S9. Power distribution. Deformation-power and thrust-power distribution along the body of (a,b) swimmer IS_η, and (c,d) swimmer SS_η. The solid red line indicates the average over a single tail-beat period (from $t = 26$ to $t = 27$), whereas the envelope denotes the standard-deviation. The silhouettes at the bottom of each panel represent the fish body.

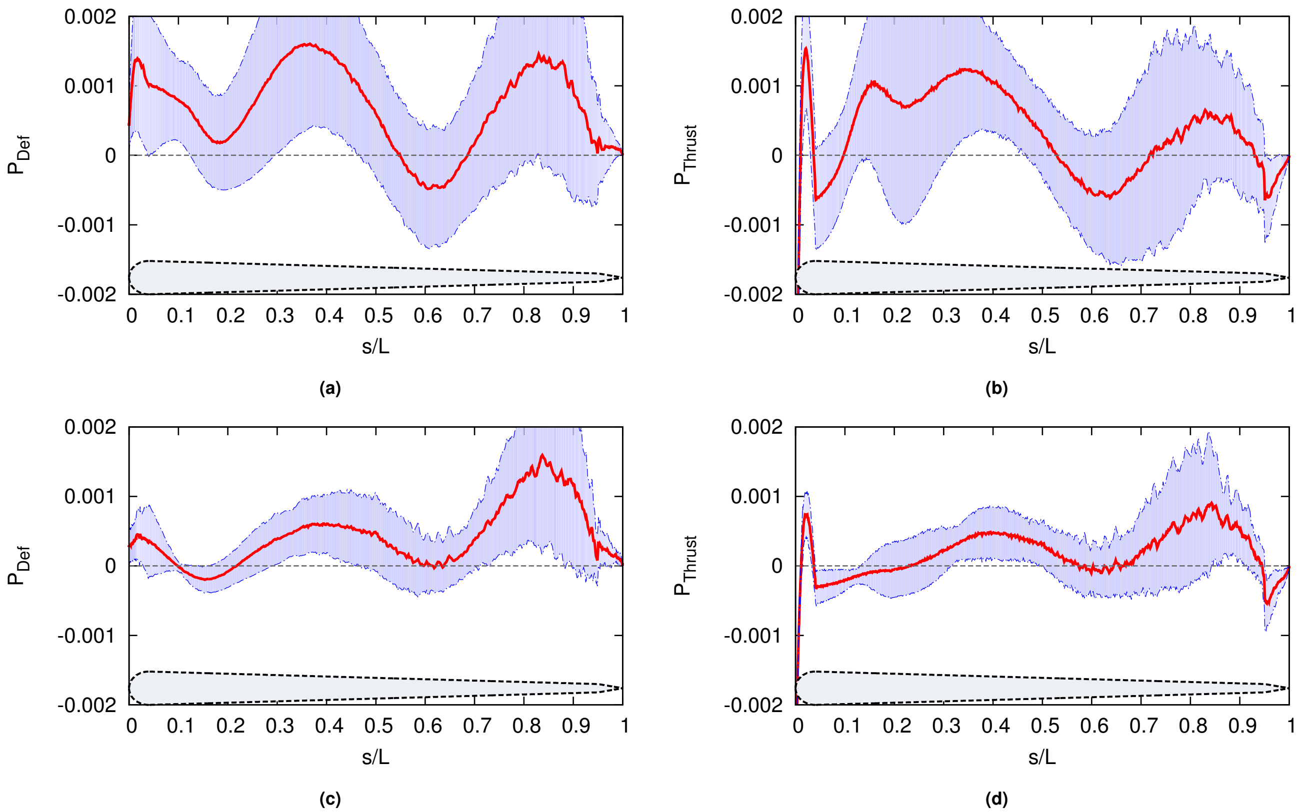

Fig. S10. Power distribution. Deformation-power and thrust-power distribution along the body of (a, b) swimmer IS_d, and (c, d) swimmer SS_d. The solid red line indicates the average over a single tail-beat period (from $t = 26$ to $t = 27$), whereas the envelope denotes the standard-deviation. The silhouettes at the bottom of each panel represent the fish body.

Table S1. Comparison of energetics metrics for the four swimmers. Averaged values computed for the data shown in SI Appendix Fig. S2. All the values shown have been normalized with respect to the corresponding value for IS_η.

	IS_η	SS_η	IS_d	SS_d
η	1.0	0.76	0.77	0.66
CoT	1.0	1.56	3.96	3.86
P_{Def}	1.0	1.41	3.90	3.28
P_{Thrust}	1.0	0.66	2.33	1.48

Movie S1. 3D simulation of three nonautonomous swimmers, in which the leader swims steadily, and the two followers maintain specified relative positions such that they interact favourably with the leader's wake. The flow-structures have been visualized using isosurfaces of the Q-criterion.[17]

Movie S2. 3D simulation of two nonautonomous swimmers, in which the leader swims steadily, and the follower maintains a specified relative position to interact favourably with the wake. The energetic-benefit for the follower is similar to that of each of the followers in Supplementary Movie S1.

Movie S3. 3D simulation of three nonautonomous swimmers, in which the leaders use a feedback controller to maintain formation abreast of each other, and the follower holds a specified position relative to the leaders. The energetic-benefit for the follower is double that of the followers in Supplementary Movies 1 and 2, as it now interacts profitably with wake-rings generated by both the leaders.

Movie S4. 2D simulation of a pair of swimmers, in which the leader swims steadily, and the follower (IS_η) takes autonomous decisions to interact favourably with the wake. The upper panel (labelled 'ω') shows the vorticity field generated by the swimmers, whereas the second panel (labelled 'v') shows the lateral flow-velocity. The smart-swimmer appears to synchronize the motion of its head with the lateral flow-velocity, which allows it to increase its swimming-efficiency. The lower panels show the energetics metrics, namely, the swimming efficiency η, the thrust-power P_{Thrust}, the deformation-power P_{Def}, and the Cost of Transport (CoT).

Movie S5. 2D simulation of a pair of swimmers, where the leader performs random actions, and the follower takes autonomous decisions to benefit from the flow-field. The smart-follower, which was trained with a steadily-swimming leader, is able to adapt to the erratic leader's behaviour without any further training. Remarkably, the follower chooses to interact deliberately with the wake in order to maximize its long-term swimming-efficiency, even though it has the option to swim clear of the unsteady flow-field.

Movie S6. A qualitative comparison between swimmer IS_η and a real fish following a leader. We observe that the motion of IS_η resembles that of the live follower quite well. The leader in the simulation executes random turns after every few tail-beat cycles, and the follower responds to changes in range and bearing, similarly to Supplementary Movie S4.

Movie S7. Detailed view of the flow-field around smart-swimmer IS_η. The top panel shows the vorticity field in colour and velocity vectors as black arrows. The middle panels show the swimming-efficiency and the deformation-power. The distribution of thrust-power and deformation-power along the swimmer's left- ('lower') and right-lateral ('upper') surfaces are shown in the lower panels, and depict how these quantities depend on wake-interactions.

References

1. Coquerelle M, Cottet GH (2008) A vortex level set method for the two-way coupling of an incompressible fluid with colliding rigid bodies. *J. Comput. Phys.* 227:9121–9137.
2. Rossinelli D, et al. (2015) MRAG-I2D: Multi-resolution adapted grids for remeshed vortex methods on multicore architectures. *J. Comput. Phys.* 288:1–18.
3. Verma S, Abbati G, Novati G, Koumoutsakos P (2017) Computing the force distribution on the surface of complex, deforming geometries using vortex methods and brinkman penalization. *Int. J. Numer. Meth. Fluids* 85(8):484–501.
4. Chorin AJ (1968) Numerical solution of the Navier-Stokes equations. *Math. Comp.* 22:745–762.
5. Rossinelli D, et al. (2013) 11 pflop/s simulations of cloud cavitation collapse in *High Performance Computing, Networking, Storage and Analysis (SC), 2013 International Conference for.* (IEEE), pp. 1–13.
6. Gholami A, Hill J, Malhotra D, Biros G (2015) AccFFT: A library for distributed-memory FFT on CPU and GPU architectures. *arXiv preprint arXiv:1506.07933.*
7. Tytell ED, Lauder GV (2004) The hydrodynamics of eel swimming. *J. Exp. Biol.* 207:1825–1841.
8. van Rees WM, Gazzola M, Koumoutsakos P (2013) Optimal shapes for anguilliform swimmers at intermediate reynolds numbers. *J. Fluid Mech.* 722:R3 1–12.
9. Sutton RS, Barto AG (1998) *Reinforcement learning: An introduction.* (MIT press, Cambridge, MA, USA).
10. Bertsekas DP (1995) *Dynamic programming and optimal control.* (Athena scientific Belmont, MA) Vol. 1.
11. Mnih V, , et al. (2015) Human-level control through deep reinforcement learning. *Nature* 518:529–533.
12. Hochreiter S, Schmidhuber J (1997) Long short-term memory. *Neural Comput.* 9:1735–1780.
13. Kingma DP, Ba J (2014) Adam: A method for stochastic optimization. *arXiv preprint arXiv:1412.6980 [cs.LG].*
14. Graves A, Schmidhuber J (2005) Framewise phoneme classification with bidirectional LSTM and other neural network architectures. *Neural Netw.* 18:602–610.
15. Novati G, et al. (2017) Synchronisation through learning for two self-propelled swimmers. *Bioinspir. Biomim.* 12:036001.
16. van Rees WM, Gazzola M, Koumoutsakos P (2015) Optimal morphokinematics for undulatory swimmers at intermediate Reynolds numbers. *J. Fluid Mech.* 775:178–188.
17. Hunt JCR, Wray AA, Moin P (1988) Eddies, streams, and convergence zones in turbulent flows in *Studying Turbulence Using Numerical Simulation Databases, 2. Report CTR-S88.* pp. 193–208.